Using Multiple Geophysical Methods to Refine a Stratigraphic Conceptual Site Model at a Nuclear Waste Site

Judy Robinson*, James St. Clair, Jon Thomle, Piyoosh Jaysaval, Joaquin Cambeiro, Kelsey Peta, Frederick Day-Lewis, Rob D. Mackley
**corresponding author, Judith.robinson@pnnl.gov*
Pacific Northwest National Laboratory, Richland, Washington (USA)

Abstract
At contaminated sites, there is a critical reliance on conceptual site models of which a key component is the geologic framework model (GFM), which is used to build predictive fate and transport modeling in support of remediation goals. We detail an ongoing study at a nuclear waste site (Hanford Site, Washington, USA) where surface geophysical methods were used to complement existing borehole information and to help site new boreholes to update and refine the GFM. Ground-based electrical resistivity tomography (ERT), time-domain electromagnetics (TEM), and seismic data was acquired on the Hanford Site's Central Plateau, where the presence of a hydraulically transmissive subsurface feature, or paleochannel, was suspected but uncertain based on contaminant concentrations at sparsely located boreholes. To assess and compare ERT, TEM, and seismic geophysical datasets, co-located data was acquired in an area where the existing GFM was more certain. Surrounding the suspected paleochannel, ERT and seismic refraction tomography showed similar subsurface structures consistent with a channelized feature. While TEM interpretation was limited in the suspected paleochannel area due to a thick resistive top layer and high electromagnetic noise, TEM showed greater utility in a different area where these factors were less prevalent. Based on the results of quasi-3D ERT inversions, we propose updates to the GFM, including identifying a paleochannel. Further, we evaluate the utility of geophysical methods and examine lessons learned that will be used as a basis for continued characterization efforts to support site management decisions and implementation efforts.

Highlights
- Geophysical methods were used for site characterization of stratigraphic structure.
- Co-located geophysical surveys provided an integrated characterization approach.
- Geophysical surveys must consider site-specific conditions.

Keywords: site characterization, electrical resistivity tomography, seismic refraction, time-domain electromagnetics, paleochannels

1. Introduction
Management of contaminants on complex sites requires a significant amount of characterization to support remediation decisions and implementation (Murray et al. 2005). Hydrogeological characterization can be expensive and time-consuming and require many sampling points to adequately interpolate subsurface structure and hydraulic properties. Traditional characterization sampling methods such as drilling of boreholes often provide small-scale, discrete measurements (Binley et al. 2015). Despite these challenges, this characterization information is critical to support remediation goals and predictive fate and transport modeling used to manage these sites. Of particular importance at contaminated sites is the identification of paleochannels, which are buried remnant stream beds that have been filled with coarser gravel and sand material to create

high hydraulic conductivity zones. These features can act as preferential groundwater flow pathways, and therefore, exert a strong influence on contaminant transport (Bjornstad et al. 2010; Xu et al. 2021; Zhi et al. 2021). In addition, paleochannels can form a historical record of past flood events, which could be useful for regional planning and/or emergency management (Upadhyay et al. 2021). Characterization of these features is complicated by limited access to the subsurface. In arid and semi-arid regions with a thick unsaturated zone and a deep water table, characterization can be even more challenging (Wellman et al. 2013).

Geophysical methods have the potential to provide characterization information at large-scale interrogation volumes and can complement information derived from well samples. Electrical, electromagnetic (EM) and seismic methods are often recognized as good candidates for site hydrogeological characterization (Foti 2013; Clement 2021) because they are sensitive to changes in subsurface porosity and moisture; furthermore, electrical and EM methods are sensitive to chemical composition (i.e., total dissolved solids) of pore fluids. However, as a result of these multiple dependencies, a fundamental problem of geophysical measurements is that the interpretation can be ambiguous (Wagner and Uhlemann 2021), impacted by more than one physical property of interest. This has led many researchers to combine multiple geophysical methods for integrated site characterizations (Carnevale and Hager 2005; Clifford and Binley 2010; Vilhelmsen et al. 2018), which constrains the interpretation and thus imparts more confidence to the resulting conceptual site models.

The Hanford Site (Washington State, USA) is a 1500-km^2 legacy nuclear waste site where geophysical methods have been used to interpret hydrostratigraphy including paleochannels. Electrical resistivity tomography (ERT) was used to identify surface water-groundwater exchange locations along the Columbia River shoreline, adjacent to the Hanford Site (Johnson et al. 2012; Wallin et al. 2013; Johnson et al. 2015), and to identify stratigraphic structure to approximately 300 m depth (Robinson et al. 2022, 2022a). Seismic reflection was used to determine the depth to a basalt layer (Hyde et al. 2011) and airborne frequency-domain electromagnetics (FEM) (Cummins 2010; Jaysaval et al. 2021) has been used to identify subsurface stratigraphy. In addition, integrative geophysical studies have combined ground-based FEM and 2D ERT to identify geologic contacts and ground-truth airborne FEM datasets (CHPRC 2010). Seismic refraction, 2D ERT and time-domain electromagnetics (TEM) soundings were used to position a future groundwater monitoring well by locating transmissive groundwater pathways and the depth to a basement basalt layer (CHPRC 2012). Geophysical imaging at the Hanford Site fills in spatial gaps between well locations, and there is an ongoing need for this information to construct and update the site geologic framework model (GFM). Building on previous knowledge, the goal of this study was to integrate previous ERT data (Robinson et al. 2022, 2022a) with newly collected ERT, seismic refraction tomography, and TEM data to refine and provide information for the Hanford Site GFM. Co-located geophysical surveys were first collected in an area where the GFM interpretation was more certain due to higher borehole coverage to provide a basis for comparing geophysical imaging techniques in a less-well-defined area. Then, geophysical surveys were conducted in an area where few wells are located, compared to borehole stratigraphic interpretations, and then used to identify stratigraphic structure, the location of paleochannels, and other stratigraphic features that could potentially impact fate and transport models. The information from this integrated approach will be used to site new wells and realize an alternative GFM and its impacts on contaminant transport to downstream receptors such as the Columbia River.

2. Study Area

The focus area of this geophysical study is within the Central Plateau, an area covering approximately 194 km^2 near the center of the Hanford Site (Fig. 1). The Central Plateau contains the 200 East and West Areas, which at one time housed five chemical separation buildings and other facilities that separated and recovered plutonium and other nuclear materials. Large quantities of liquid wastes containing radionuclides and hazardous chemicals were generated during process operations, and an estimated 1.7 billion m^3 has been discharged to the ground (Last et al. 2009). The Central Plateau has a deep vadose zone (~80 m depth), and much of this contamination still resides above the water table. Groundwater flow across the site is generally from west to east, discharging into the Columbia River, which surrounds the site to the north and east. Geophysical imaging was mainly focused between the 200 Areas.

The GFM represents an interpretation of the 3D physical arrangement of hydrostratigraphic units, which directly influences the distribution and migration of contaminants. The information in the GFM is critical to support fate and transport modeling, and therefore, is updated by Hanford Site soil and groundwater remediation contractors as new information or interpretations become available. Two GFM models are used on the Hanford Site to support modeling efforts: (1) a regional model designated as the Hanford South GFM (Hammond and Lupton 2015; Wigginton 2022), which encompasses the saturated and unsaturated units on the Hanford Site; and (2) a vadose zone model of the Central Plateau (Springer 2018). The geologic units in these models are almost entirely based on borehole geologic and geophysical logs. Therefore, where there are sparsely located or no boreholes, as is the case between the 200 Areas, the uncertainties increase in the GFM interpretation.

Although there are sparsely located boreholes between the 200 West and East Areas, a paleochannel has been inferred from a borehole cross section across the 200 West Area (Fig A-5 in DOE 2002,) that suggests a complex erosional pattern and monitoring of contaminant concentrations in groundwater at wells surrounding this area. An extensive groundwater monitoring program exists at Hanford (DOE 2020), and this provides indirect evidence of subsurface connectivity. However, not knowing the location and geometry of this hypothesized paleochannel creates uncertainty associated with the attenuation of contaminants migrating from the Central Plateau (Demirkanli and Freedman 2021). This uncertainty is reflected in estimates of contaminant travel times from the Central Plateau to the Columbia River, which range from a few decades to a century or more (Gephart 2003). Geophysical methods can provide a first line of evidence as to the existence of a paleochannel and can also help site future monitoring wells.

The major hydrostratigraphic units at the Hanford Site from upper (shallower) to lower (deep) are the Hanford formation (Hf), the Cold Creek unit (CCu), the Ringold Formation and the Columbia River Basalt (Ba) group. The Hf consists of glacio-fluvial deposits associated with cataclysmic Ice Age flooding; the CCu contains alluvial, fluvial and paleosol deposits; and the Ringold Formation consists of alluvial and lacustrine deposits. These units are further subdivided based on proximity to ancient river systems and floodpaths into member of Taylor Flat (Rtf); member of Wooded Island, Unit E (Rwie); and member of Wooded Island, Unit A (Rwia). A generalized stratigraphic overview is shown in Fig. SM1, and readers are encouraged to review Martin (2010) and DOE (2002) for more details. Paleochannels are associated with the incision of Hf channels at different depths within Ringold and CCu sediments, and in some instances scouring down to the basalt. These channels were later filled in with poorly sorted Hf sands and gravels and are thought to represent highly permeable pathways to transport contaminants within the groundwater.

Geophysical surveys were performed between the 200 Areas in a region where a paleochannel was suspected but few wells were available to verify its existence and location. ERT data was previously collected along linear transects and analyses and interpretations were performed by Robinson et al. (2022, 2022a). In this previous study, data was collected along eight transects totaling 18.5 linear kilometers. The interpretation was limited to 2D and relied on limited supporting data. This work utilizes the data from Robinson et al. (2022, 2022a) and further investigates the findings of this previous study by collecting and analyzing: (1) additional ERT datasets; (2) co-located seismic data; and (3) TEM data near the ERT and seismic transects (Fig. 1; Table 1).

Previously, the ERT results were compared to a site-wide GFM model (Hammond and Lupton 2015). However, given the sparsity of wells in the areas where geophysical surveys have been acquired, there is uncertainty from the inherent interpolation of various datasets. Therefore, this work focuses on direct comparison of the geophysical results to stratigraphic interpretations at well locations.

Table 1 Geophysical surveys analyzed in these investigations.

Method	**Area/Line Designation**	**Details**
ERT	FY20,1,2,3,3a,4,5,6	Robinson et al. (2022, 2022a)
ERT	Line 5a	2,775 m, 112 electrodes
ERT	Line 7	2,775 m, 112 electrodes
ERT	Line 8	3,175 m, 128 electrodes
ERT	Line 9	3,175 m, 128 electrodes
Seismic	Line 3	480 geophone, 159 shots
Seismic	Line 4	456 geophones, 358 shots
Seismic	Line A1-P	264 geophones, 225 shots
TEM	tTEM 1	2,300 linear m
TEM	tTEM 2	4,985 linear m
TEM	tTEM 3	1,540 linear m
TEM	tTEM 4	6,700 linear m

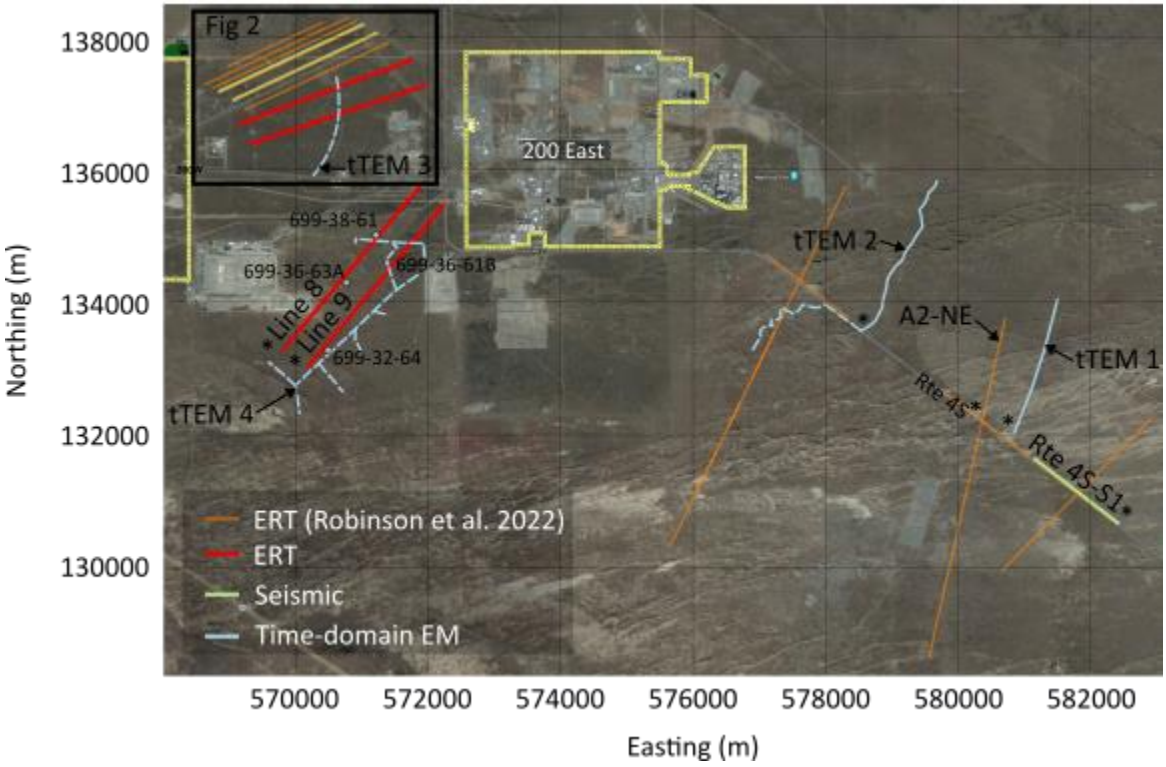

Fig. 1 Map of geophysical surveys collected on the Central Plateau (Hanford Site, Washington, USA) in Washington State Plane coordinates. Previously acquired ERT surveys are annotated as Robinson et al. (2022) and all other surveys on this map were acquired as part of this study. Dashed blue lines indicate transects with poor data quality. Asterisks indicate the starting point (X=0) along the lines shown in the Results.

3. Methods

3.1 Electrical Resistivity Tomography

Electrical resistivity (the inverse of electrical conductivity (EC), referred to herein as conductivity) quantifies a material's ability to conduct an electric current. EC depends on the bulk intrinsic electrical properties of the material's three phases (solid, liquid and gas) and their spatial arrangement (Binley and Slater 2020). Specifically, EC is a function of porosity, fluid conductivity and pore connectivity. ERT is an active source geophysical method that uses an array of electrodes to image subsurface bulk EC. Four-electrode measurements are commonly used. In each measurement, current (I) is injected between one electrode pair and the resulting electrical potential (i.e., the voltage, ΔV) is measured across a second (or multiple) electrode pair(s). To solve for subsurface spatial distributions of bulk EC, raw ERT data of resistance values ($\Delta V/I$, ohm) are analyzed using an inversion algorithm. Different electrode combinations and spacings are commonly used to optimize imaging resolution to meet site objectives. While the advantages of 3D versus 2D ERT have been well documented (Chambers 2002; Wilkinson et al. 2006), acquiring 3D ERT data is costly and time-consuming (Rucker et al. 2009), especially for larger (e.g., kilometer-scale) areas. As a result, researchers have used quasi-3D approaches where data is collected along 2D transects and processed in 3D. Approaches

include 2D data acquisition along multiple parallel transects (Oglivy et al. 2002; Robinson et al. 2015) or multiple orthogonal lines (Rucker et al. 2009). Less equipment and time are required for quasi-3D data acquisition; thus, the quasi-3D approach provides a cost-effective but limited form of 3D interpretation. In this study, previously and newly collected 2D ERT data along multiple parallel lines was processed using the 3D modeling and inversion code E4D (Johnson et al. 2010; Johnson 2014).

The ERT measurement sequence used a four-electrode array including nested (Wenner-Alpha and Schlumberger, multiple-gradient) and dipole-dipole configurations (Ward 1988). A 64-electrode cable was used with 25-m electrode spacing (1,575 m total length). Small, intermediate and larger offset dipoles were used to provide optimal resolution for both shallow and deep structures to the extent possible. The same 6,500 2D ERT measurements were collected along each 64-electrode cable transect. Data quality checks consisted of removing measurements with high contact resistances (>15 kohm), low current injections (<2 mA) and high stacking deviations (>5%). A full set of reciprocal measurements (where source and receiver electrodes are swapped) were collected, and measurements with > 20% reciprocal error were culled. Overlapping "roll along" surveys were conducted (Dahlin 1996) to extend lines beyond the 1,575 m length. For these field surveys, the amount of overlap varied depending on field logistics and required lateral extensions; however, the typical overlap used was 50%. Overlapping surveys resulted in duplicate measurements; redundant measurements were averaged unless there was > 20% deviation, in which case they were culled.

Two separate quasi-3D inversions were performed after results of an inversion that used all ERT data simultaneously in a quasi-3D inversion showed a poor data fit and proved unstable. The first inversion, referred to herein as the North (N) survey, used ERT data from lines 1-5 from Robinson et al. (2022, 2022a) and Robinson et al. (2020). The second inversion, herein referred to as the South (S) survey, used ERT data from lines 5a, 6 and 7. In addition, 3D inversions were performed for 2D ERT lines 8 and 9 because they were located too far from the other ERT transects to be included in the other quasi-3D inversions. Table 2 summarizes the inputs used in the inversions.

Metallic infrastructure can detrimentally impact and reduce the utility of ERT images. Johnson and Wellman (2015) proposed a solution within E4D whereby metallic infrastructure with a known location is included in the forward modeling. To determine the impact of metallic infrastructure on this ERT data, inversions were evaluated without the inclusion of metallic infrastructure. Where high-conductivity anomalies at known locations of metallic infrastructure were evident, a subsequent inversion was performed that included this infrastructure using the implementation of Johnson and Wellman (2015). Table 2 shows the inputs where metallic infrastructure was included in the inversion.

Table 2 Inputs used in the E4D inversions.

ERT Inversion	# Measurements	# Electrodes	# Mesh Elements
Quasi-3D North (N) Lines FY20, 1,2,3,3a,4,5 (Robinson et al. 2020, Robinson et al. 2022, 2022a)	59,261	639	2,321,128
Quasi-3D South (S) Lines 5a, 6 (Robinson et al. 2022), 7	32,872	334	1,371,710
Line 8	14,184	128	1,538,290
Line 9	13,974	128	1,506,968

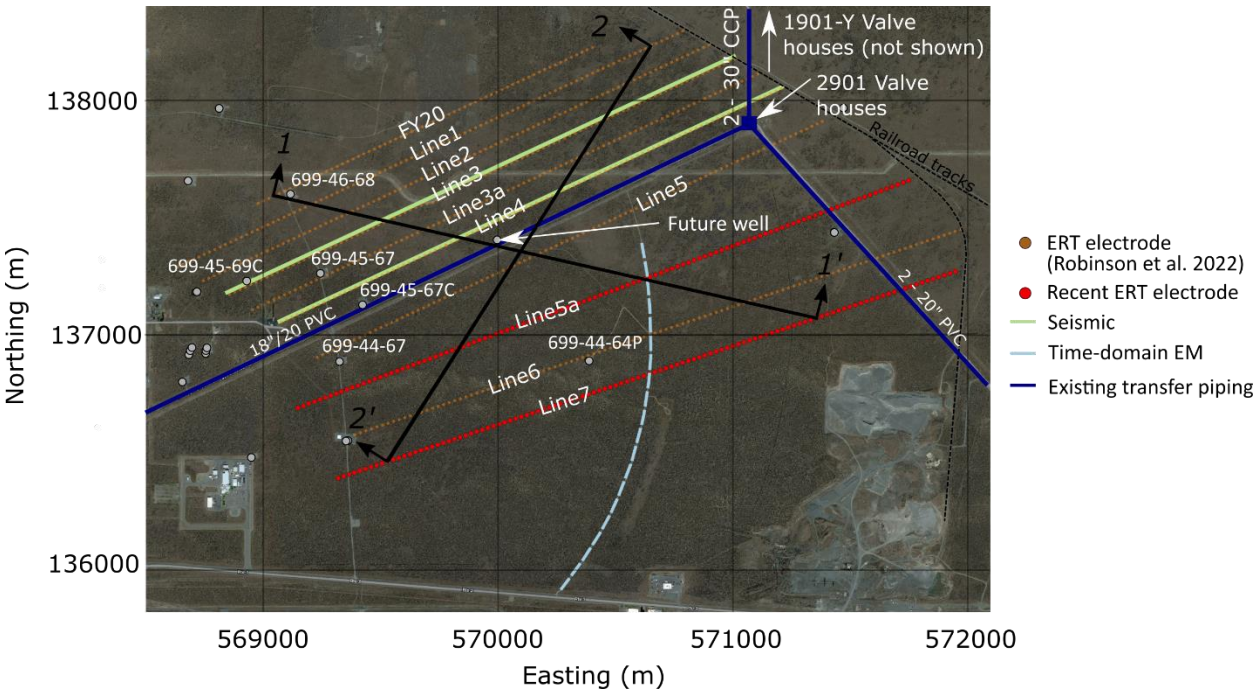

Fig. 2 ERT transects included in two independent quasi-3D ERT inversions. Co-located ERT and seismic surveys were collected on lines 3 and 4. Wells are shown as gray circles. Wells with stratigraphic interpretations (Hammond 2015) are labeled. Modified from Robinson et al. (2022).

The model domain is discretized using an unstructured tetrahedral mesh in E4D. Hanford LIDAR data (https://phoenix.pnnl.gov) was used to incorporate surface topography. The inversion uses a deterministic, iterative reweighted least squares method where the data analysis is posed as a regularized inverse problem. The iterative scheme minimizes an objective function composed of two terms: (1) the data misfit, in a least-squares sense; and (2) model complexity. The two terms are weighted relative to each other according to a regularization coefficient, which is adjusted during the computation to achieve a data fit consistent with the expected errors (Johnson et al. 2010). The data is weighted according to the reciprocals of its standard errors. A relative error of 5% was used in these inversions, which considers discretization and reciprocal data errors. To discourage model overfitting to very small resistance measurements, a relative error was added to each measurement. Inversions were fit to a χ^2 value equal to 1 (Binley and Slater 2020). The objective function term for model complexity promotes smoothness through

minimization of second-derivative operator between adjacent mesh elements calculated using nearest-neighbor differences.
ERT image resolution is a function of survey geometry, the electrical properties of the imaged volume, measurement noise and regularization used in the inversion (Day-Lewis et al. 2005). In this work, sensitivity was assessed as J^tJ where J is the Jacobian matrix which is equal to the derivative of each measurement with respect to the bulk EC in each finite element volume. To visualize this value, the sensitivity was normalized by each element volume.

3.2 Seismic

Seismic surveys measure the propagation of elastic waves in the subsurface and allow for estimates of the compressional (Vp) and shear (Vs) velocities. These velocities are sensitive to lithology, porosity and confining pressure; however, Vp increases when saturated, while Vs is relatively unchanged in the presence of fluids (e.g., Mavko et al. 2020). Seismic velocities were previously measured at the Hanford Site for the geologic units in the study area (Redpath 2007; Rohay and Brouns 2007; Hyde et al. 2011; Linneman et al. 2021) (Table 3). These measurements suggest that seismic velocity can reliably differentiate the slower Hf and CCu from the faster Ringold Formation and Ba group.

Table 3 Seismic velocity measurements of Hanford geologic units.

Geologic Formation	**Vp (m/s)**	**Vs (m/s)**
Hf	*†500-1,500 (dry)	*200-800
CCu	*1,200-2,000 (dry)	*600-800
Rwia	*3,000-4,000 (saturated)	*2,000-2,200
Ba group	*‡3,500-5,500 (saturated)	*2,200-2,600

*Rohay and Brouns (2007), †Linneman et al. (2020), ‡Hyde et al. (2011)

Seismic data was collected using a 96-channel Geometrics GEODE system. The data was recorded using 4.5-Hz vertical component geophones spaced 5 m apart. A 5-kg sledgehammer was used as the seismic source. Measurements were recorded for 1.5 seconds at a sample rate of 2,000 Hz after each "shot," i.e., strike of the sledgehammer. Shot spacing ranged between 5 and 15 m, and four to eight sledgehammer strikes were stacked at each source location to increase the signal-to-noise ratio. To maintain offsets of at least 250 m, source positions were reoccupied after moving geophones ahead on the profile. Maximum offsets ranged between 250 and 475 m and provide the data necessary to characterize the depth to Ba and lateral variations in Ba Vp. This recording geometry is also suitable for obtaining Vs from multi-channel analysis of surface waves (MASW) (Pasquet and Bodet 2017).
Vp images were obtained from inversion of manually selected first arrival travel times. The travel-time data was inverted with a 2D tomography code written in MATLAB (St. Clair 2015). The code parameterizes the model as a grid of cells with a fixed horizontal dimension of 2.5 m and a constant slowness (inverse of velocity) within each cell. Vertical cell dimensions increase linearly with depth from 2.5 to 5 m. Rays are traced using the shortest path algorithm (Moser 1991), and structural constraints are implemented using first-derivative operators in the vertical and horizontal directions. An iterative, reweighted least-squares approach (Ajo-Franklin et al.

2006) was used during the inversion to apply an L1 norm on model structure and encourage sharp boundaries between regions with strong velocity contrasts (such as the top of basalt). The approach is to obtain a model update with the usual L2 norm constraint on model structure, calculate the spatial derivatives, then reweight the structural constraint with the inverse of the spatial derivatives. This process is iterated until the L1 norm on model structure, as measured by the first-order derivative operator, stops increasing. The effect is to reduce the smoothness penalty in regions where a large model gradient is preferred by the data and to increase the penalty in regions where small model gradients are preferred. Misfit and model statistics for Vp images are listed in Table 4.

Table 4 Summary of Vp tomography modeling and results.

Profile	**Number of Data**	**# Model Parameters**	**Root Mean Squared Misfit (ms)**
Route 4S	8,523	12,672	2
Line 3	18,153	47,775	3.4
Line 4	12,560	37,040	4

Vs was extracted from Rayleigh wave dispersion using a method similar to that presented by Pasquet and Bodet (2017). Dispersion images for shot-spread pairs distributed about the same midpoint were stacked and dispersion curves were interpreted from the resulting images. Shot-spread pairs were chosen to enhance low-frequency (deep) information with wide aperture data and high-frequency (shallow) information with narrower aperture data. Dispersion curves were extracted every 20 m along each profile.

The dispersion curves were inverted for 1D Vs profiles using MATLAB (St. Clair 2015). The models were parameterized as a stack of homogenous layers over a half-space with thicknesses linearly increasing from 1 m at the surface to 3 m at a depth of 80 m. An initial model was derived from the experimental dispersion curves assuming that the Rayleigh wave velocity is ~0.88Vs and the corresponding depth to that velocity is about half the wavelength (phase velocity / frequency), similar to the recommendations of Foti et al. (2017). Theoretical dispersion curves were calculated using the propagator matrix approach described in Aki and Richards (2002), and an iterative linearized inversion with smoothness constraints was performed until the misfit reduction was less than 1%. Sensitivities of each model parameter to the root mean squared data misfit were derived by summing the columns of the Jacobian matrix. Those model parameters with less sensitivity are masked in the final images.

3.3 Time-domain Electromagnetics

TEM is an active source geophysical method that can be used to image subsurface bulk EC. A towed time-domain electromagnetic (tTEM) system designed by Aarhus University (Auken et al. 2019) was used to collect the TEM data. This system is designed to provide a lateral resolution of about 10 m and a vertical depth of investigation ranging from the top 2–3 m to about 50–70 m, depending on the subsurface EC, and is sensitive to electrically conductive targets. The system consists of a 2- by 4-m^2 single-turn coil acting as a transmitter (Tx coil) and a 0.56- by 0.56-m^2 multi-turn coil with an effective area of 5 m^2 acting as a receiver (Rx coil). The Tx and Rx coils are horizontal loops separated by 9 m (coil center-to-center) in an out-of-loop configuration. The

apparatus is mounted on sleds for stability and smooth towing behind an all-terrain vehicle (ATV). The battery and electronic components are mounted on the back of the ATV. The tTEM system collects hundreds of measurements every second while the ATV moves with an operational speed of 15–20 km/h.

tTEM data was processed and inverted to obtain the distribution of bulk EC in the subsurface. The processing and inversion of the data was performed with the Aarhus Workbench software, which uses the moderately parallelized AarhusInv code (Auken et al. 2015) using OpenMP directives for modeling and inversion of TEM data. The processing step involves automatic and manual removal of noise from various sources (e.g., capacitive couplings from metallic infrastructures, power line noise, random noise) and thereafter stacking over a predefined window, usually about 10 m, to get averaged sounding (stacked) data. The stacked data is then used for the inversion, which is carried out with a laterally or spatially constrained inversion scheme assuming 1D layered models of the subsurface. Depending on the data collection, either along a single line or along multiple parallel lines, the inversion generates a pseudo 2D or 3D model showing the distribution of subsurface EC. For a detailed description of the tTEM system and its data processing, see Auken et al. (2019).

tTEM data was collected along existing gravel roadways as to not disturb native vegetation. It was presumed that metallic infrastructure (e.g., pipelines) was not present in these areas (Fig. 1). Southeast of 200 East, tTEM data was acquired near previously collected ERT lines (Robinson et al. 2022) in two data acquisitions, labeled tTEM 1 and tTEM 2 in Fig. 1. Between the 200 Areas, near lines 1-7 (Fig. 2), there were few roadways for data collection and data acquisition was limited to a single transect referred to as tTEM3. Further south between the 200 Areas, tTEM data was collected along roadways near lines 8 and 9, referred to as tTEM4 (Fig. 1).

4. Results

4.1 Co-located Geophysical Surveys

Data from the three geophysical methods were compared along Route 4S on the Hanford Site (Fig. 1), where borehole stratigraphic interpretations constrain the GFM better than in other areas with less borehole coverage. Robinson et al. (2022) observed a strong agreement between the GFM and ERT images in this region (**Error! Reference source not found.**). Comparing the data from different geophysical methods to this well-defined area of the GFM promotes confidence in interpreting the geophysical data where the GFM is defined by limited borehole control.

First, we compare TEM to ERT. An attempt was made to co-locate data along Route 4S; however, the data was extremely noisy, likely due to infrastructure below the roadway. In lieu of this location, data was collected along tTEM1, where there is a gravel roadway, and compared to ERT line A2-NE (refer to Fig. 1 for locations). Despite the physical separation, and differences in depth of investigation, both images display a low bulk EC layer to an elevation of approximately 110 m and similar bulk EC values throughout the images (Fig. 3).

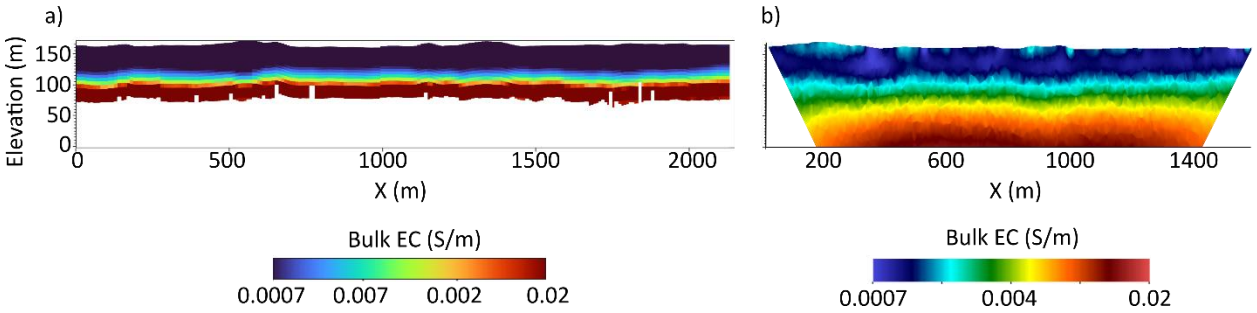

Fig. 3 A comparison of a) tTEM1 and b) ERT line A2-NE sections in the 600 Area. The cutoff portion at depth in a) are areas of low resolution where the interpretation is less certain.

Co-located seismic and ERT data was collected along 4S-S1 (refer to Fig. 1 for location). Co-located Vp, Vs and bulk EC are shown in Fig. 4. The color scale represents Vp (Fig. 4a) and Vs (Fig. 4b) and the bulk EC is shown as contours. Note that the shallowest elevation shown in Fig. 4 corresponds to the seismic depth of investigation, and the bulk EC resolution extends to the elevations shown in Fig. 3. The water table at 120 m elevation aligns well with Vp=1,500 m/s, e.g., the speed of sound in water (Greenspan and Tschiegg 1957). In Fig. 4a, Vp shows horizontal structure that matches bulk EC well; however, Vp is more sensitive to the water table boundary. Vp also shows lateral variability that is not present in the bulk EC contours. This could be due to resolution differences between the seismic and ERT surveys and/or a larger seismic velocity gradient than bulk EC gradient.
The Vs image (Fig. 4b) shows a shallow (~25 m depth) contact, which is consistent with the bulk EC and Vp results. The consistency between the three approaches provides confidence in model interpretation. Compared to tTEM and ERT, the seismic method offers a way to look at shallow (40-50 m depth) stratigraphic structure where there is limited borehole coverage. In addition, the seismic images reveal lateral variability in the velocity, potentially providing insight into stratigraphic structure not delineated in the GFM (refer to Fig SM2a).

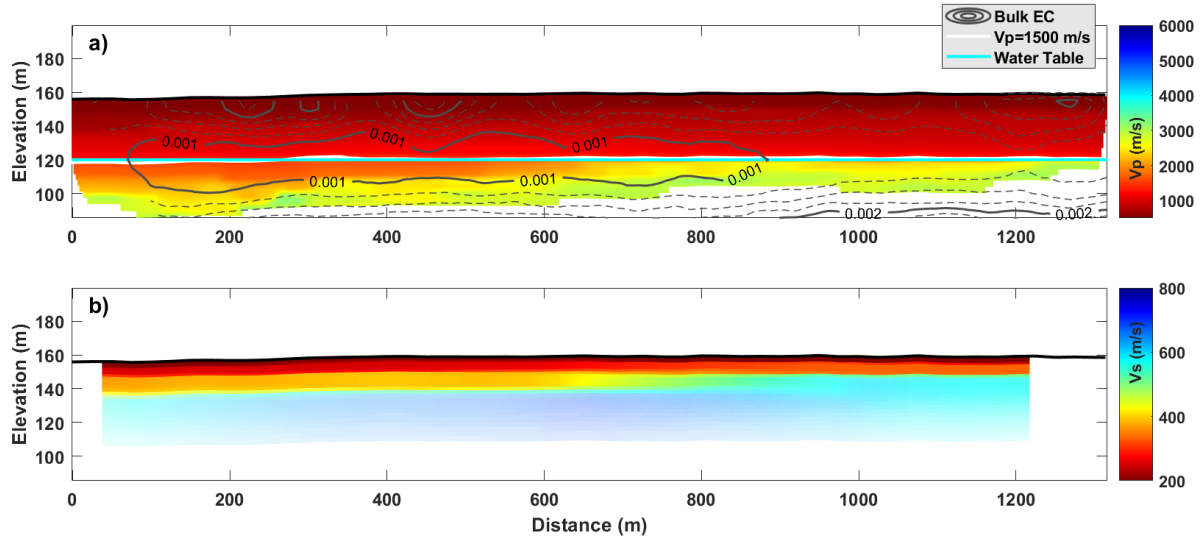

Fig. 4 Co-located seismic a) Vp and bulk EC (S/m) and b) Vs along 4S-S1. Refer to Fig. 1 for location and Fig. SM2 for ERT image comparison to the GFM.

4.2 Electrical Resistivity Tomography

ERT results of the quasi-3D inversions are presented as select 2D slices (Figs. 5-7) and in plan view (Fig. 8). These images reveal a shallower low bulk EC layer which extends deeper on the northeast ($X \geq 1500$ m) side of the ERT lines. In plan view (Fig. 8), the low bulk EC feature extends from the northwest to the southeast and is flanked by higher bulk EC regions. Where available, borehole stratigraphy from well log characterizations (Springer 2019; Wigginton 2022) are shown alongside N and S quasi-3D ERT images. Several stratigraphic boundaries coincide with electrical contrasts. For example, the CCu layer coincides with a low bulk EC layer (Fig. 5), and one of the stratigraphic units encountered near the lower boundary of the boreholes (either the Rwia or Ba group) is coincident with a transition to higher EC. In the S inversion (Fig. 6), the top stratigraphic units (Hf, Rwie, Rwia) coincide with a low bulk EC; however, there is no distinction in the ERT between these units. Like the N inversion, the lower stratigraphic units are coincident with a transition to high EC. It is expected that the Rlm would have a high bulk EC because of the fine-grained silt and clays that can retain more moisture; however, this thin layer is not distinguishable in the ERT, likely due to the smoothness constraints applied in the inversion modeling. Cross sections 1-1' and 2-2' are shown in Fig. 7, which indicates that generally the low bulk EC layer gets deeper on the southern ends of these sections.

Plan view slices at different elevations show the combined N and S quasi-3D images (Fig. 8). As the elevation decreases, there is a low bulk EC region flanked by two higher bulk EC regions. A borehole cross section across the 200 West Area (Fig A-5 in DOE 2002) suggests a complex erosional pattern while the GFM predicts higher permeability sediments between the 200 Areas (Springer 2019; Wigginton 2022). Based on the location and shape of the low bulk EC feature shown in the ERT images, we hypothesize that the low bulk EC region in Fig. 5 represents paleochannel sediments with higher hydraulic conductivity.

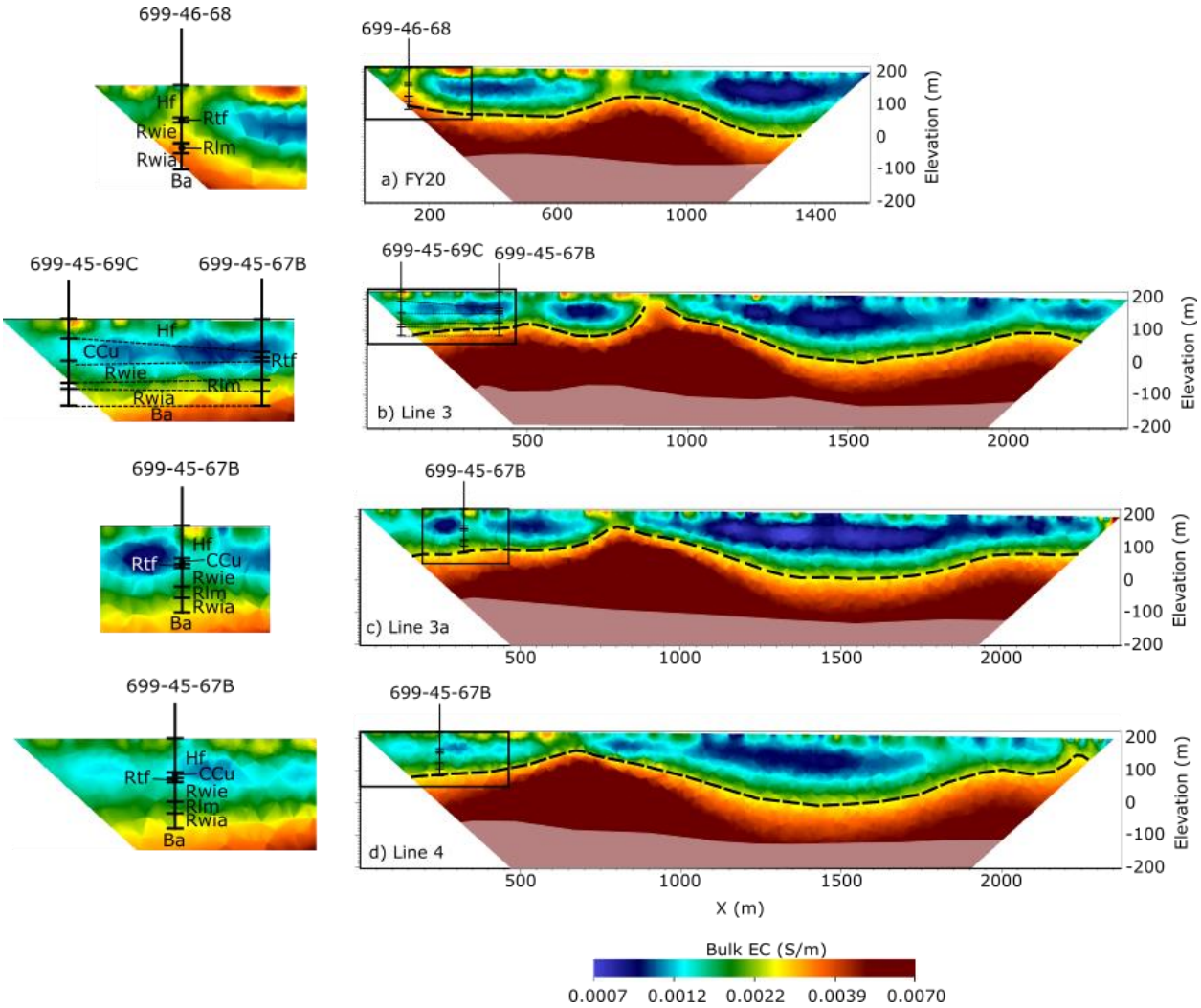

Fig. 5 Selected 2D slices from the N inversion showing the borehole stratigraphic interpretations (Springer 2019; Wigginton 2022) alongside quasi-3D images for ERT lines a) FY20, b) line 3, c) line 3a and d) line 4. The shaded portion of the images represents areas of low sensitivity that may not be as well-resolved. The bold dashed black lines represent a bulk EC value = 0.0025 S/m. ERT lines are oriented from southwest (X=0) to northeast.

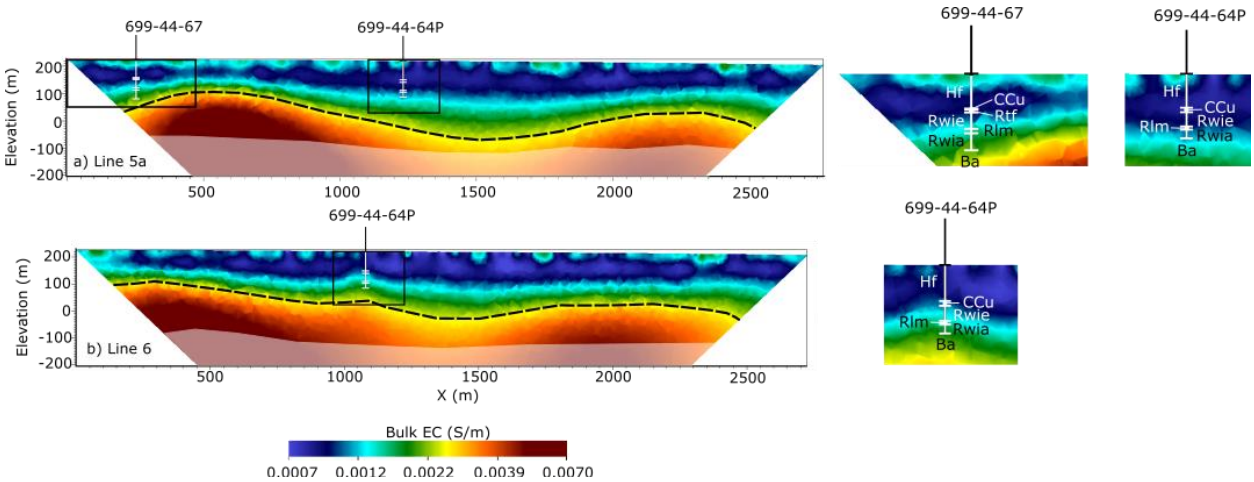

Fig. 6 Selected 2D slices from the S inversion showing the borehole stratigraphic interpretations (Springer 2019; Wigginton 2022) alongside quasi-3D images for ERT lines a) line 5a and b) line 6. The shaded portion of the images represents areas of low sensitivity that may not be as well-resolved. The bold dashed black lines represent a bulk EC value = 0.0025 S/m. ERT lines are oriented from southwest (X=0) to northeast.

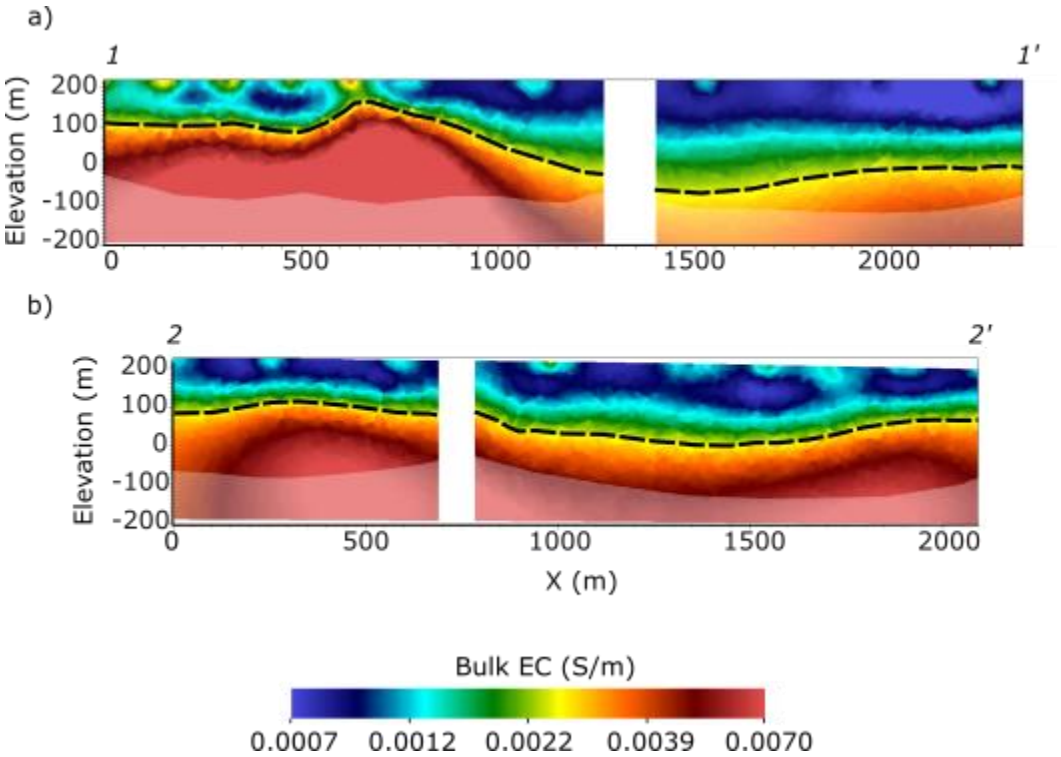

Fig. 7 Cross-sections 1-1'(a) and 2-2' (b) from the combined quasi-3D ERT N and S inversions. Refer to Fig. 1 for locations. The shaded portion of the images represent areas of low sensitivity that may not be as well-resolved. The bold dashed black lines represent a bulk EC value = 0.0025 S/m.

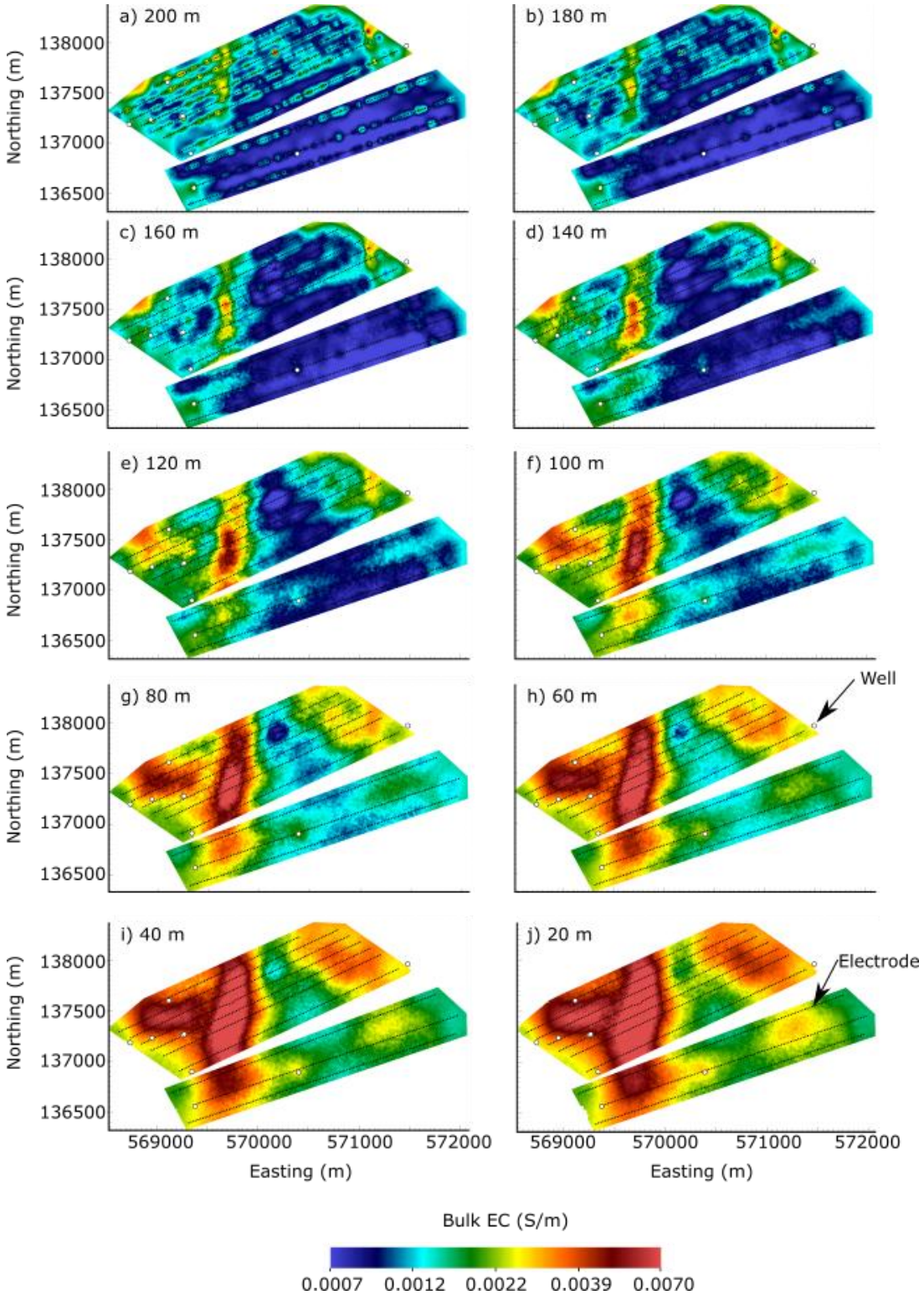

Fig. 8 Plan view slices of N and S quasi-3D ERT inversions with elevations ranging from a) 200 m to j) 20 m.

ERT images for lines 8 and 9 (Fig. 9) show layers slightly dipping to the northeast (refer to Fig. 1). The main transfer pipeline between the 200 Areas was identified during field work which consists of six stainless steel 7.62 cm (3-inch) diameter pipelines within a concrete encasement. These pipelines have a strong localized impact on the ERT image (Fig. 9a). In addition, there is a high-conductivity feature surrounding well 699-32-64 along line 9 (Fig. 9b). Including this as metallic infrastructure reduced the high bulk EC halo surrounding this area. Attempts to include the transfer line as metallic infrastructure resulted in a limited improvement, likely due the large diameter of these pipelines and the fact that the location was not precisely known. In the image shown, there was no metallic infrastructure used in the inversion modeling. Comparing to borehole stratigraphic interpretations (Springer 2019; Wigginton 2022), Hf coincides with a low EC along both transects and the lower Ba boundary of 699-36-61B coincides with a high-conductivity contrast.

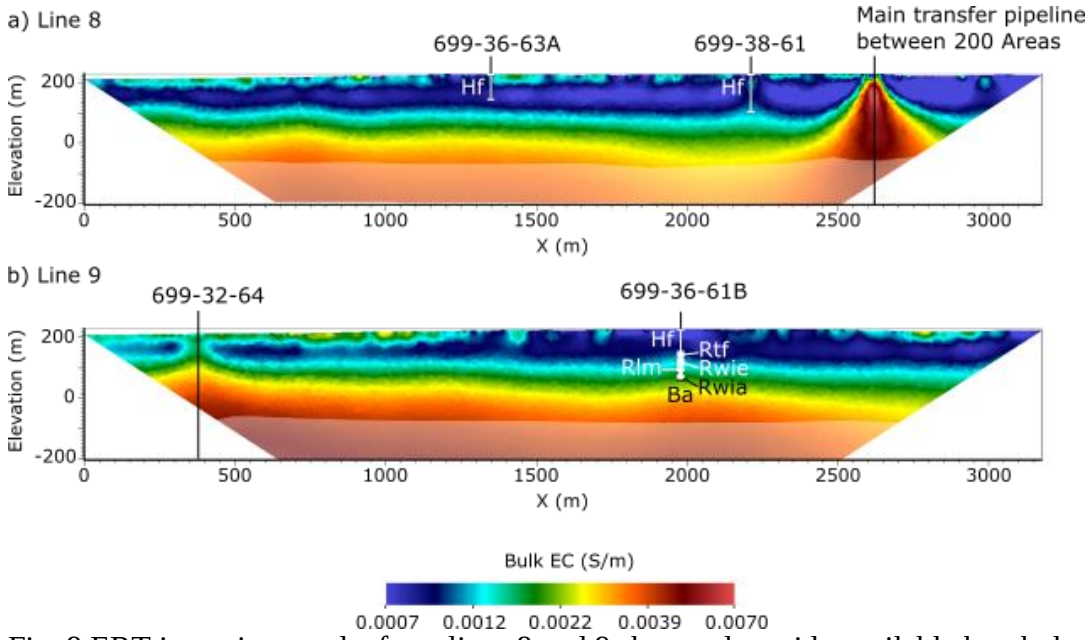

Fig. 9 ERT inversion results from lines 8 and 9 shown alongside available borehole stratigraphic interpretations (Hammond 2015; Springer 2019; Wigginton 2022). The shaded portions of the images represent areas of low sensitivity that may not be as well-resolved.

4.3 Seismic

Vp inversion results for lines 3 and 4 (Fig. 10a, c) show comparable structure to the ERT results. Vp in this area ranges from ~500 m/s near the surface to >4,500 m/s at the lower limit of data sensitivity. The ERT results are overlain as contours on Fig. 10a, c. The highlighted 0.0025 S/m ERT contour shows a similar trend to seismic velocities >4,500 m/s but shows a deeper trough on the northeast half of the profiles. Both seismic profiles show a thick (~100 m) section of Vp < 2,000 m/s, consistent with Hf and CCu (refer to Table 3). The northeast half of both profiles (x > ~1,200 m) shows a sharp transition from Vp < 2,000 m/s to Vp > 4,500 m/s, possibly corresponding to the transition from CCu to Ba. On the southwestern portion of the profiles, the boundary is more diffuse, suggesting the presence of materials with velocities intermediate between CCu and Ba. Ringold sediments were identified in wells 699-45-69C and 699-45-67B

(Springer 2019; Wigginton 2022). The transistion from a diffuse to a sharper Vp boundary at depth occurs at x~1,000 m on line 3 and x~700 m on line 4. This coincides with a shallowing of the conductive feature imaged by the ERT.
The MASW-derived Vs images (Fig. 10b, d) highlight shallower structure showing a 35- to 50-m-thick section of Vs < 600 m/s overlying Vs~800 m/s; this is consistent with a transition from Hf to CCu sediments. The interpreted Hf formation, which is supported by the boundaries observed in 699-45-69C and 699-45-67B, appears to thin toward the northeast and displays lateral velocity variations that likely represent changes in grain-size distribution and/or porosity.

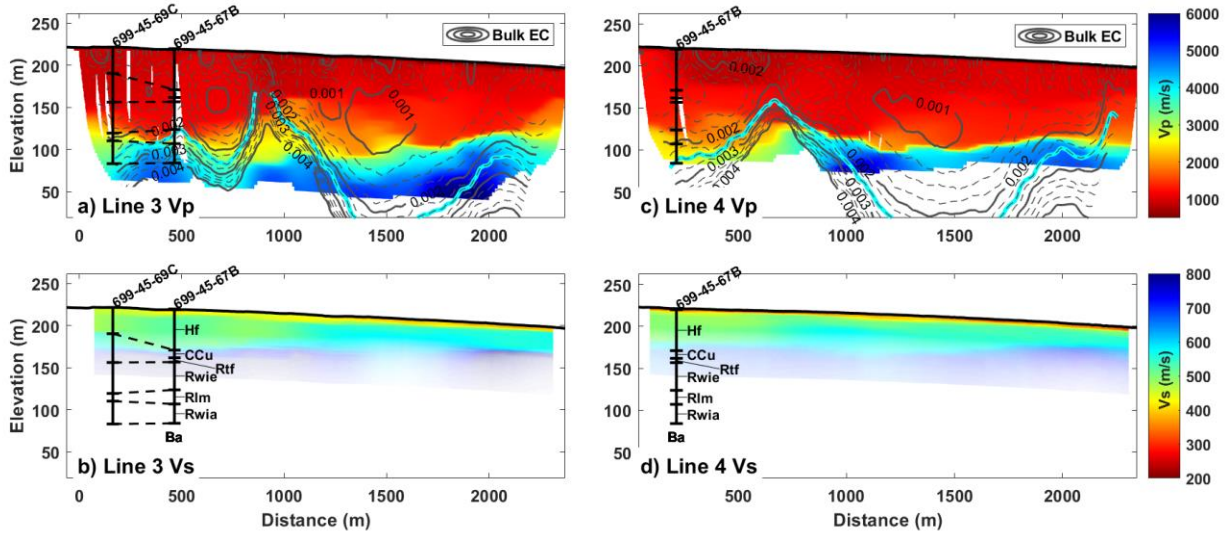

Fig. 10 Seismic velocity results along lines 3 and 4. ERT contours are overlain on the Vp results (a and c) with the 0.0025 S/m contour highlighted in cyan. MASW-derived Vs results are shown in panels b and d. Borehole stratigraphic interpretations (Springer 2019; Wigginton 2022) for wells 699-45 69C and 699-45-67B are also shown. Lines 3 and 4 are oriented from southwest (X=0) to northeast.

4.4 TEM

Raw data for TEM transects tTEM2, tTEM3 and tTEM4 is shown in Fig. 11. Each colored line in the plots is the time derivative of the vertical component of the secondary magnetic field ($VA^{-1}m^{-2}$) for one time gate. A major source of noise in the tTEM data is the coupling with nearby infrastructure. The coupling noise can be recognized as unusual data patterns, e.g., crossing of individual time gate recordings, oscillatory recordings or significantly large contrasts in the field magnitudes. The coupling noise notably affected the quality of tTEM data collected along line tTEM4 (Fig. 11c). Along and surrounding line tTEM4, signal boxes were found in the field, and it was presumed that this infrastructure contaminated the data shown in Fig. 11c. The only data that was of sufficient quality to invert was line tTEM2 (Fig. 11a). Data for line tTEM3 has a low signal magnitude and attempts to invert this data produced images with a poor data fit. A low signal magnitude is consistent with the presence of a highly resistive surficial layer, to which the tTEM instrument is relatively insensitive; this is consistent with the ERT images. Fig. 11

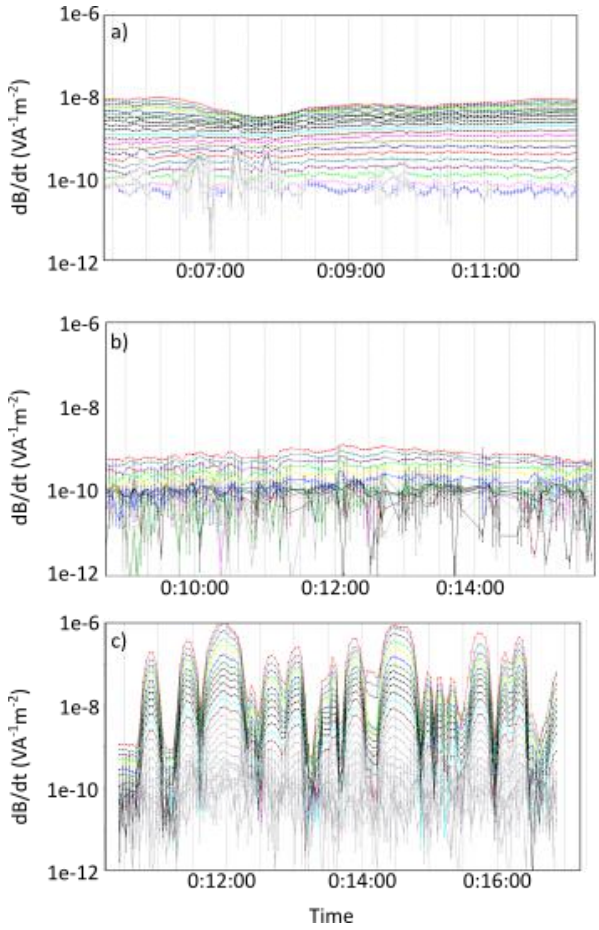

Fig. 11 Raw tTEM data shown for a) tTEM2, b) tTEM3 and c) tTEM4 (refer to Fig. 1 for locations).

The EC image along tTEM2 is shown in Fig. 12 with borehole stratigraphic interpretations from surrounding wells (Hammond 2015). The image is cut off at depth (below the high-conductivity red layer) to remove low-resolution areas. tTEM soundings that were removed from this analysis due to poor data quality are shown as blank areas for the entire elevation of the image. Hf and CCu units have a lower bulk EC than Ringold units, and the strongest contrast is between the Hf and CCu units. The Hf and CCu units are shallower in this area than between the 200 Areas according to the ERT images, presumably due to the higher data quality.

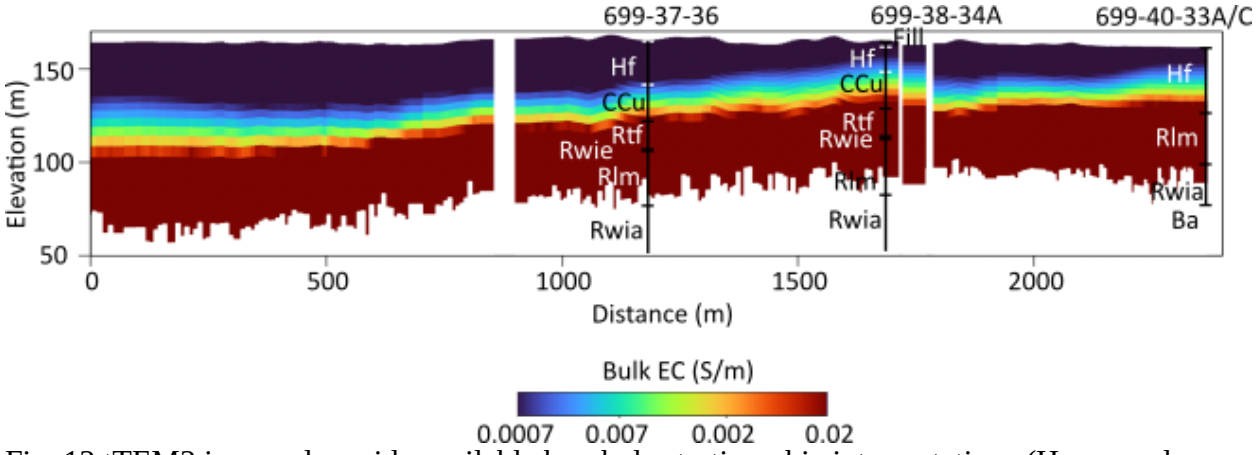

Fig. 12 tTEM2 image alongside available borehole stratigraphic interpretations (Hammond 2015).

5. Discussion and Conclusions

Integrated multi-method and multi-resolution geophysical investigations provide valuable information for environmental site characterization as demonstrated in past studies (Binley and Slater 2020; Day-Lewis et al. 2017; Robinson et al. 2020; Singha et al 2022). Here, ERT, seismic and TEM geophysical methods were used to collect ground-based data at the Hanford Site in an ongoing study to investigate stratigraphic structure hundreds of meters below the ground surface to help inform the GFM and identify optimum locations for new characterization and monitoring wells. The approximate depth of investigations for ERT, TEM, seismic refraction and MASW are 250 m, 80 m, 120 m and 70 m, respectively. ERT with large (25-m) electrode spacing was used to image bulk EC hundreds of meters below the surface. ERT was supplemented with TEM lines, which are faster and less laborious to collect. Seismic refraction tomography and MASW surveys were used to image Vs and Vp at shallower depths compared to ERT, providing another line of evidence toward stratigraphic structure and lateral delineation within shallower geologic units. TEM was consistent with ERT in a well-defined area, but noisy data and a deep resistive layer limited its utility. Independently, these methods provide information at a scale not obtainable with traditional borehole sampling. Together combining geophysical datasets provided multiple lines of evidence to better resolve subsurface structure that influence contaminant migration and inform the optimum placement of characterization boreholes and groundwater monitoring wells. This will lead to more efficient groundwater monitoring and remediation, cost savings, and ultimately reduced time for cleanup and site closure.

A deep, low bulk EC feature hypothesized to be a paleochannel was delineated between the 200 Areas, and this agreed with seismic refraction imaging. The question then becomes: how can we incorporate this information within GFM development with limited ground-truthing information when the parameter of interest is a physical or hydrologic property (e.g., lithology, particle size, compaction, saturation or hydraulic conductivity) rather than a geophysical property (e.g., seismic velocity or bulk EC)? Petrophysical models such as Archie's law (Archie 1942) can be used to convert bulk EC to, for example, porosity; however, this estimation is complicated by variable geophysical image resolution (Day-Lewis et al. 2005) and uncertainty in the petrophysical parameters.

Rather than converting geophysical estimates to parameters of interest, we used the geophysical results to identify the extent of an interpreted paleochannel by selecting a bulk EC value to represent a boundary between higher and lower permeable units. This was not meant to supply a definitive set of boundaries; however, it provides a means to investigate an alternative GFM between the 200 Areas and select a new site for a borehole. A value of 0.0025 S/m was chosen based on the ERT images (Figs. 5-8), the overlay of available borehole stratigraphic interpretations (Figs. 5-7), and the comparison with seismic tomograms (Fig. 10). Additional information from future sources (for example, a 1D ERT profile within a borehole or well) could allow for refinement of this selected bulk EC value. Fig. 13 shows the elevation at each location where the bulk EC is equal to 0.0025 S/m. Close to well 699-44-64P there is a region of relatively higher bulk EC and it may be that the metallic well casing is the cause of this feature (refer to Fig. 6b). However, the visualization of deeper, low bulk EC regions allows for conceptualization of a potential transmissive feature between the 200 Areas. Note there are limited wells within the deeper low bulk EC region (Fig. 13) to provide ground truthing and this image provides a first-line of evidence towards stratigraphic structure in this area. This conceptualization will be used to support improved decision-making of the GFM for long-term management.

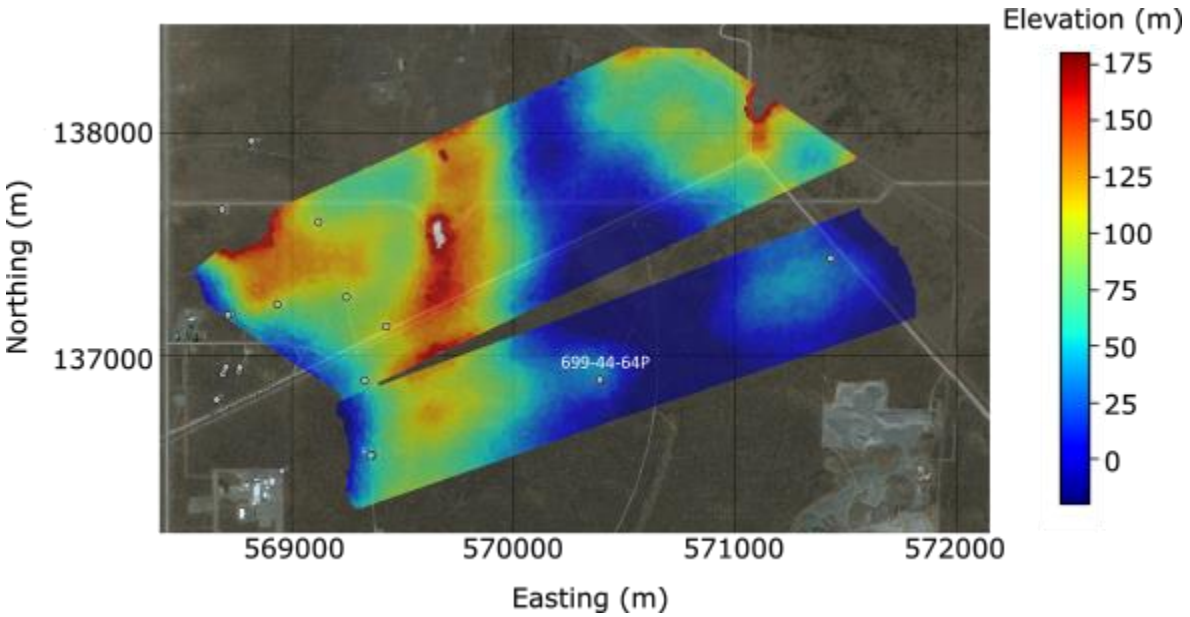

Fig. 13 Conceptualization of an interpreted paleochannel between the 200 Areas where the elevation is shown for a bulk EC=0.0025 S/m. Existing wells are shown as gray circles.

While geophysical images provide many benefits, they cannot replace borehole information. Bulk EC, Vp and Vs are influenced by several physical and hydrologic properties, which can make the geophysical interpretation non-unique. Interpreted stratigraphic units in boreholes help constrain the geophysical interpretation; however, when comparing the two, it should be recognized that (1) a stratigraphic unit can have textural and grain-size differences that can impact the geophysical properties, and (2) the geophysical datasets were collected at different scales and therefore have different resolutions. For these surveys, bulk EC and Vp can provide large-scale differentiation between Hf and lower units (50-80 m deep) with 25-m electrode and 5-m geophone spacing. For shallower features (<20 m), higher resolution is required, and closer

electrode spacing and shot gathers from closer-spaced geophones are required to enable delineation. Geophysical survey design and method selection, therefore, must consider study goals, the dimensions and depth of targets, and site conditions.

Statements and Declarations

This document was prepared under the Deep Vadose Zone – Applied Field Research Initiative at Pacific Northwest National Laboratory. The Pacific Northwest National Laboratory is operated by Battelle Memorial Institute for the U.S. Department of Energy under Contract DE-AC05-76RL01830.

Data Availability Statement

The datasets generated during and/or analyzed during the current study are available from the corresponding author on reasonable request.

Competing/Conflicting Interests

There are no competing or conflicting interests for any authors directly or indirectly related to this work.

Funding

Funding information is reported under the 'Statements and Declarations' section.

Authors Contributions

Conceptualization: Judith Robinson; Methodology: Judith Robinson, James St. Clair, Formal analysis: Judith Robinson, James St. Clair, Piyoosh Jaysaval; Field investigation: Jonathan Thomle, James St. Clair, Joaquin Cambeiro, Kelsey Peta; Writing – original draft preparation: Judith Robinson, James St. Clair, Piyoosh Jaysaval; Writing – review and editing: Judith Robinson, James St. Clair, Piyoosh Jaysaval, Fred Day-Lewis; Funding acquisition: Rob Mackley; Supervision: Judith Robinson, Fred Day-Lewis; All authors read and approved the final manuscript.

References

Ajo-Franklin JB, Minsley BJ, Daley TM (2006) Applying compactness constraints to seismic traveltime tomography. Massachusetts Institute of Technology

Aki K, Richards PG (2002) Quantitative seismology. University Science Books, New York

Archie GE (1942) The electrical resistivity log as an aid in determining some reservoir characteristics. Petroleum Transactions of AIME 146: 54-62. https://doi.org/10.2118/942054-G

Auken E, Christiansen AV, Kirkegaard C, Fiandaca G, Schamper C, Behroozmand AA, Binley A, Nielsen E, Effersø F, Christensen NB, Sørensen K, Foged N, Vignoli G (2015) An overview of a highly versatile forward and stable inverse algorithm for airborne, ground-based and borehole electromagnetic and electric data. Exploration Geophysics 46: 223-235. https://doi.org/10.1071/eg13097

Auken E, Foged N, Larsen JJ, Lassen KVT, Maurya PK, Dath SM, Eiskjaer TT (2019) tTEM — A towed transient electromagnetic system for detailed 3D imaging of the top 70 m of the subsurface. Geophysics 84: E13-E22. https://doi.org/10.1190/GEO2018-0355.1

Binley A, Hubbard S, Huisman J, Revil A, Robinson D, Singha K, Slater L (2015) Understanding of subsurface processes over multiple scales. Water Resources Research 51: 3837-3866. https://doi.org/10.1002/2015WR017016

Binley A, Slater L (2020) Resistivity and induced polarization: Theory and applications to the near-surface earth. Cambridge University Press

Bjornstad B, Thorne P, Williams B, Last G, Thomas G, Thompson M, Ludwig J, Lanigan D (2010) Hydrogeologic model for the gable gap area, Hanford Site, Pacific Northwest National Laboratory Richland, WA

Carnevale M, Hager J (2005) Integrated geophysical method for characterizing hydro-stratigraphy at a contaminated site. SEG Technical Program Expanded Abstracts 20051152-1155

Chambers RO, O. Kuras, JC, J. (2002) 3D electrical imaging of known targets at a controlled environmental test site. Environmental Geology 41: 690-704. https://doi.org/10.1007/s00254-001-0452-4

CHPRC (2010) Testing ground based geophysical techniques to refine electromagnetic surveys north of the 300 Area, Hanford, Washington, CH2M Hill Plateau Remediation Company Richland, WA (United States)

CHPRC (2012) Integrated surface geophysical investigation results at liquid effluent retention facility, 200 East Area, Hanford, Washington, CH2M Hill Plateau Remediation Company Richland, WA (United States)

Clement WP (2021) Geophysical site characterization In: Alderton D and Elias S (ed) Encyclopedia of Geology, (2nd Edition). Academic Press, pp 805-814

Clifford J, Binley A (2010) Geophysical characterization of riverbed hydrostratigraphy using electrical resistance tomography. Near Surface Geophysics 8: 493-501. https://doi.org/10.3997/1873-0604.2010035

Cummins GD (2010) Intepretation of airborne electromagentic and magnetic data in the 600 area, CH2MHill Plateau Remediation Company Richland, WA (United States)

Dahlin T (1996) 2D resistivity surveying for environmental and engineering applications. First Break 14. https://doi.org/10.3997/1365-2397.1996014

Day-Lewis FD, Singha K, Binley AM (2005) Applying petrophysical models to radar travel time and electrical resistivity tomograms: Resolution-dependent limitations. Journal of Geophysical Research B: Solid Earth 110: 1-17. https://doi.org/10.1029/2004JB003569

Day-Lewis FD, Slater LD, Robinson J, Johnson CD, Terry N, Werkema D (2017) An overview of geophysical technologies appropriate for characterization and monitoring at fractured-rock sites. Journal of Environmental Management 204:2 709-720.

Demirkanli I, Freedman V (2021) Adaptive site management strategies for the Hanford central plateau groundwater, Pacific Northwest National Laboratory Richland, WA (USA)

DOE (2002) Standardized stratigraphic nomenclature for post-ringold-formation sediments within the central Pasco basin Richland, Washington

DOE (2020) Hanford Site groundwater monitoring report for 2020

Foti S (2013) Combined use of geophysical methods in site characterization In: (ed) Geotechnical and Geophysical Site Characterization: Proceedings of the 4th International Conference on Site Characterization ISC-4, 1. Taylor & Francis Books Ltd, pp 43-61

Foti S, Hollender F, Garofalo F, Albarello D, Asten M, Bard P-Y, Comina C, Cornou C, Cox B, Di Giulio G, Forbriger T, Hayashi K, Lunedei E, Martin A, Mercerat D, Ohrnberger M, Poggi V, Renalier F, Sicilia D, Socco V (2017) Guidelines for the good practice of surface wave analysis: a product of the InterPACIFIC project. Bulletin of Earthquake Engineering 16: 2367-2420. https://doi.org/10.1007/s10518-017-0206-7

Gephart R (2003) A short history of Hanford waste generation, storage, and release, Pacific Northwest National Laboratory Richland, Washington

Greenspan M, Tschiegg CE (1957) Speed of sound in water by a direct method. Journal of Research of the National Bureau of Standards 59.4: 249-254.

Hammond T, Lupton D (2015) Development of the Hanford south geologic framework model, Hanford Site, Washington. ECF-HANFORD-13-0029, Revision 2, CH2M Hill Plateau Remediation Company, Richland, Washington

Hammond TB (2015) Development of the Hanford south geologic framework model, Hanford Site, Washington

Hyde ER, Speece MA, Link CA, Repasky TR, Thompson MD, Miller SF (2011) A seismic landstreamer survey at the Hanford Site, Washington, U.S.A. Environmental and Engineering Geoscience 17: 227-239. https://doi.org/10.2113/gseegeosci.17.3.227

Jaysaval P, Robinson JL, Johnson TC (2021) Stratigraphic identification with airborne electromagnetic methods at the Hanford Site, Washington. Journal of Applied Geophysics 192: 104398. https://doi.org/10.1016/j.jappgeo.2021.104398

Johnson T (2014) E4D : A distributed memory parallel electrical geophysical modeling and inversion code User Guide - Version 1.0, Pacific Northwest National Laboratory Richland, Washington

Johnson TC, Slater LD, Ntarlagiannis D, Day-Lewis FD, Elwaseif M (2012) Monitoring groundwater-surface water interaction using time-series and time-frequency analysis of transient three-dimensional electrical resistivity changes. Water Resources Research 48: 1-13. https://doi.org/10.1029/2012WR011893

Johnson TC, Versteeg R, Thomle J, Hammond G, Chen X, Zachara J (2015) Four-dimensional electrical conductivity monitoring of stage-driven river water instrusion: Accounting for water table effects using a transient mesh boundary and conditional inversion constraints. Water Resources Research 51: 1-20. https://doi.org/10.1016/0022-1694(68)90080-2

Johnson TC, Versteeg RJ, Ward A, Day-Lewis FD, Revil A (2010) Improved hydrogeophysical characterization and monitoring through parallel modeling and inversion of time-domain resistivity and induced-polarization data. Geophysics 75. https://doi.org/10.1190/1.3475513

Johnson TC, Wellman D (2015) Accurate modelling and inversion of electrical resistivity data in the presence of metallic infrastructure with known location and dimension. Geophysical Journal International 202: 1096-1108. https://doi.org/10.1093/gji/ggv206

Last G, Bjornstad B, Thorne P, Mackley R, Horner J, Lanigan D, Parker K, Williams B (2009) Hydrologeology of the Hanford Site central plateau - A status report for the 200 west area, Pacific Northwest National Laboratory Richland, Washington

Linneman DC, Strickland CE, Mangel AR (2021) Compressional wave velocity and effective stress in unsaturated soil: Potential application for monitoring moisture conditions in vadose zone sediments. Vadose Zone Journal 20. https://doi.org/10.1002/vzj2.20143

Martin CJ (2010) Overview of Hanford hydrogeology. Hanford Site Groundwater Monitoring and Performance Report: 2009

Mavko G, Mukerji T, Dvorkin J (2020) The rock physics handbook. Cambridge University Press

Moser TJ (1991) Shortest path calculation of seismic rays. Geophysics 56: 59-67.

Murray CJ, Last GV, Truex MJ (2005) Review of geophysical techniques to define spatial dstribution of subsurface properties or contaminants, Pacific Northwest National Laboratory Richland, Washington

Oglivy RD, Meldrum PI, Chambers JE, Williams G (2002) The use of 3D electrical resistivity tomography to characterise waste and leachate distribution within a closed landfill, Thriplow, UK. Journal of Environmental and Engineering Geophysics 7. https://doi.org/https://doi.org/10.4133/JEEG7.1.11

Pasquet S, Bodet L (2017) SWIP: An integrated workflow for surface-wave dispersion inversion and profiling. Geophysics 82: WB47-WB61. https://doi.org/10.1190/GEO2016-0625.1

Redpath BB (2007) Downhole measurements of shear- and compression-wave velocities in boreholes C4993, C4996, C4997 and C4998 at the waste treatment plant DOE Hanford Site, Pacific Northwest National Laboratory Richland, WA (United States)

Robinson J, Johnson T, Slater L (2015) Challenges and opportunities for fractured rock imaging using 3D cross borehole electrical resistivity. Geophysics 80: E49-E61.

Robinson J, Mackley R, Rockhold M, Johnson T, Thomle J, Johnson C, Jaysaval P (2020) Geophysical methods for stratigraphic identification

Robinson J, Thomle J, McFarland D, Deters K, Rockhold M, Day-Lewis F, Freedman V (2022) Integration of large-scale electrical imaging into geological framework development and refinement. Environmental Processes 9(2), 21. https://doi.org/10.1007/s40710-022-00570-2

Robinson J, Thomle J, McFarland D, Deters K, Rockhold M, Day-Lewis F, Freedman V (2022a) Correction to: Integration of Large-Scale Electrical Imaging into Geological Framework Development and Refinement. Environmental Processes 9, 45. https://doi.org/10.1007/s40710-022-00596-6

Rohay AC, Brouns TM (2007) Site-specific velocity and density model for the waste treatment plant, Hanford, Washington, Pacific Northwest National Laboratory Richland, WA (United States)

Rucker DF, Levitt MT, Greenwood WJ (2009) Three-dimensional electrical resistivity model of a nuclear waste disposal site. Journal of Applied Geophysics 69: 150-164. https://doi.org/10.1016/j.jappgeo.2009.09.001

Singha K, Johnson TC, Day-Lewis FD, Slater LD (2022) Electrical Imaging for Hydrogeology. The Groundwater Project, Guelph, Ontario, Canada.

Springer S (2018) Model package report: Central plateau vadose zone geoframework version 1.0 Richland, WA

Springer S (2019) Central plateau vadose zone geoframework, Ch2M Hill Plateau Redmediation Company

St. Clair J (2015) Geophysical investigations of underplating at the Middle American Trench, weathering in the critical zone, and snow water equivalent in seasonal snow, Doctoral thesis submitted at University of Wyoming

Upadhyay RK, Kishore N, Sharma M (2021) Delineation and mapping of palaeochannels using remote sensing, geophysical, and sedimentological techniques: A comprehensive approach. Water Science 35: 100-108. https://doi.org/10.1080/23570008.2021.1941691

Vilhelmsen T, Marker P, Foged N, Wernberg T, Auken E, Christiansen AV, Bauer-Gottwein P, Christensen S, Høyer A-S (2018) A regional scale hydrostratigraphy generated from geophysical data of varying age, type, and quality. Water Resources Management 33: 539-553. https://doi.org/10.1007/s11269-018-2115-1

Wagner FM, Uhlemann S (2021) An overview of multimethod imaging approaches in environmental geophysics In: Schmelzbach C (ed) Advances in Geophysics, 62. Elsevier, pp 1-72

Wallin EL, Johnson TC, Greenwood WJ, Zachara JM (2013) Imaging high stage river-water intrusion into a contaminated aquifer along a major river corridor using 2-D time-lapse surface electrical resistivity tomography. Water Resources Research 49: 1693-1708. https://doi.org/10.1002/wrcr.20119

Ward S (1988) The resistivity and induced polarization methods. Symposium on the Application of Geophysics to Engineering and Environmental Problems147-189

Wellman D, Truex M, Johnson T, Bunn A, Golovich E (2013) Deep vadose zone–applied field research initiative fiscal year 2012 annual report, Pacific Northwest National Laboratory Richland, WA

Wigginton S (2022) Geologic contacts for the Hanford south geoframework model

Wilkinson PB, Chambers JE, Meldrum PI, Ogilvy RD, Caunt S (2006) Optimization of array configurations and panel combinations for the detection and imaging of abandoned mineshafts

using 3D cross-hole electrical resistivity tomography. Journal of Environmental & Engineering Geophysics 11: 213-221. https://doi.org/10.2113/JEEG11.3.213

Xu Z, Hariharan J, Passalacqua P, Steel E, Paola C, Michael HA (2021) Linking the surface and subsurface in river deltas—part 2: Relating subsurface geometry to groundwater flow behavior. Water Resources Research 57. https://doi.org/10.1029/2020wr029281

Zhi C, Cao W, Wang Z, Li Z (2021) High-arsenic groundwater in paleochannels of the lower Yellow River, China: Distribution and genesis mechanisms. Water 13. https://doi.org/10.3390/w13030338